Fault structure and kinematics of the Long Valley Caldera region, California, revealed by high-accuracy earthquake hypocenters and focal mechanism stress inversions

Stephanie Prejean,[1,3] William Ellsworth,[2] Mark Zoback,[1] and Felix Waldhauser[1,4]

Received 6 September 2001; revised 8 May 2002; accepted 24 May 2002; published 19 December 2002.

[1] We have determined high-resolution hypocenters for 45,000+ earthquakes that occurred between 1980 and 2000 in the Long Valley caldera area using a double-difference earthquake location algorithm and routinely determined arrival times. The locations reveal numerous discrete fault planes in the southern caldera and adjacent Sierra Nevada block (SNB). Intracaldera faults include a series of east/west-striking right-lateral strike-slip faults beneath the caldera's south moat and a series of more northerly striking strike-slip/normal faults beneath the caldera's resurgent dome. Seismicity in the SNB south of the caldera is confined to a crustal block bounded on the west by an east-dipping oblique normal fault and on the east by the Hilton Creek fault. Two NE-striking left-lateral strike-slip faults are responsible for most seismicity within this block. To understand better the stresses driving seismicity, we performed stress inversions using focal mechanisms with 50 or more first motions. This analysis reveals that the least principal stress direction systematically rotates across the studied region, from NE to SW in the caldera's south moat to WNW–ESE in Round Valley, 25 km to the SE. Because WNW–ESE extension is characteristic of the western boundary of the Basin and Range province, caldera area stresses appear to be locally perturbed. This stress perturbation does not seem to result from magma chamber inflation but may be related to the significant (~20 km) left step in the locus of extension along the Sierra Nevada/Basin and Range province boundary. This implies that regional-scale tectonic processes are driving seismic deformation in the Long Valley caldera. *INDEX TERMS:* 7230 Seismology: Seismicity and seismotectonics; 8164 Tectonophysics: Evolution of the Earth: Stresses—crust and lithosphere; 7280 Seismology: Volcano seismology (8419); *KEYWORDS:* Long Valley, faults, seismicity, stress, relocation

Citation: Prejean, S., W. Ellsworth, M. Zoback, and F. Waldhauser, Fault structure and kinematics of the Long Valley Caldera region, California, revealed by high-accuracy earthquake hypocenters and focal mechanism stress inversions, *J. Geophys. Res.*, *107*(B12), 2355, doi:10.1029/2001JB001168, 2002.

1. Introduction

[2] In May 1980 four **M**6 earthquakes occurred just south of the Long Valley caldera in eastern California (Figure 1), accompanied by renewed uplift of the caldera's resurgent dome. Since that time, there have been multiple discrete episodes of increased seismicity and deformation in the Long Valley area (see the work of *Hill et al.* [2002] for an overview of caldera activity). Because the caldera is located on the active western border of the Basin and Range province in a major (~20 km) left step over in the normal faults bounding the Sierra Nevada (Figure 1), ongoing activity in the region most likely results from some combination of tectonic and magmatic processes. Although high seismicity and deformation rates have led to extensive seismic and geodetic monitoring, the mechanics of the interaction between Basin and Range tectonics, the edge of the comparatively stable Sierra Nevada block (SNB), and a possible resurgence of the caldera magmatic system remain enigmatic.

[3] One clue toward understanding deformation in the Long Valley area is the existence of a stress perturbation in the vicinity of the caldera. Earthquake focal mechanism and borehole breakout analyses indicate that the minimum horizontal principal stress (Sh_{MIN}) in the resurgent dome of the caldera is oriented NE–SW [*Moos and Zoback*, 1993; *Vetter and Ryall*, 1983]. This Sh_{MIN} direction is in marked contrast with the WNW–ESE to E-W Sh_{MIN} direction characteristic of the western Basin and Range province [*Zoback*, 1989; *Bellier and Zoback*, 1995], the west moat and Mammoth Mt. areas [*Hill et al.*, 1990; *Moos and Zoback*, 1993], and the Mono/Inyo volcanic chain region [*Bursik and Sieh*, 1989], based on analyses of earthquake focal mechanisms, borehole breakouts, fault offsets, hydraulic fracturing, and the

[1]Department of Geophysics, Stanford University, Stanford, California, USA.
[2]U.S. Geological Survey, Menlo Park, California, USA.
[3]Now at U.S. Geological Survey, Menlo Park, California, USA.
[4]Now at Lamont–Doherty Earth Observatory of Columbia University, Palisades, New York, USA.

0148-0227/02/2001JB001168$09.00

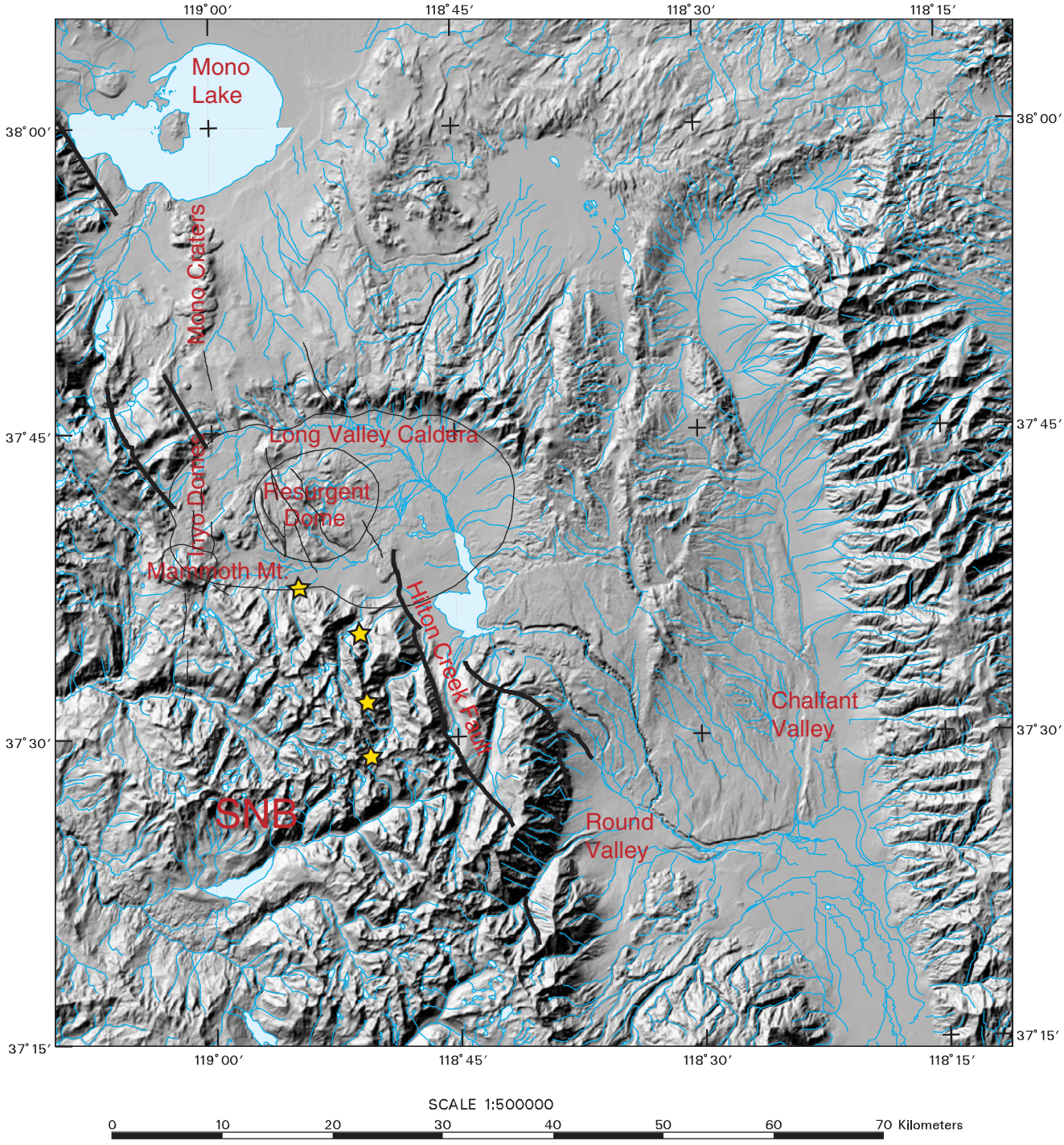

Figure 1. Shaded relief map of the Long Valley caldera area. Thin black lines designate the caldera and resurgent dome boundaries and the major faults in the Long Valley area. Thick black lines are the Sierra Nevada range bounding normal faults. Yellow stars are the May 1980 ~**M**6 earthquakes. Figure courtesy of David Hill.

alignment of young volcanic vents. Magmatically influenced earthquakes [*Dreger et al.*, 2000; *Julian et al.*, 2000] and inflation of the resurgent dome [*Savage and Cockerham*, 1984; *Langbein*, 1989; *Langbein et al.*, 1995; *Marshall et. al.*, 1997; *Battaglia et al.*, 1999] indicate that a magmatic system at depth is influencing deformation in the Long Valley area, but the exact nature of these processes, their interaction with regional tectonics, and their relationship to the observed stress perturbation are not understood.

[4] To help address these questions and better understand the geometry of the faults in the area and the sense of motion of those faults, we have carried out precise earthquake relocations and performed a series of detailed focal mechanism stress inversions to map stress variations. By combining the precisely imaged fault orientations with

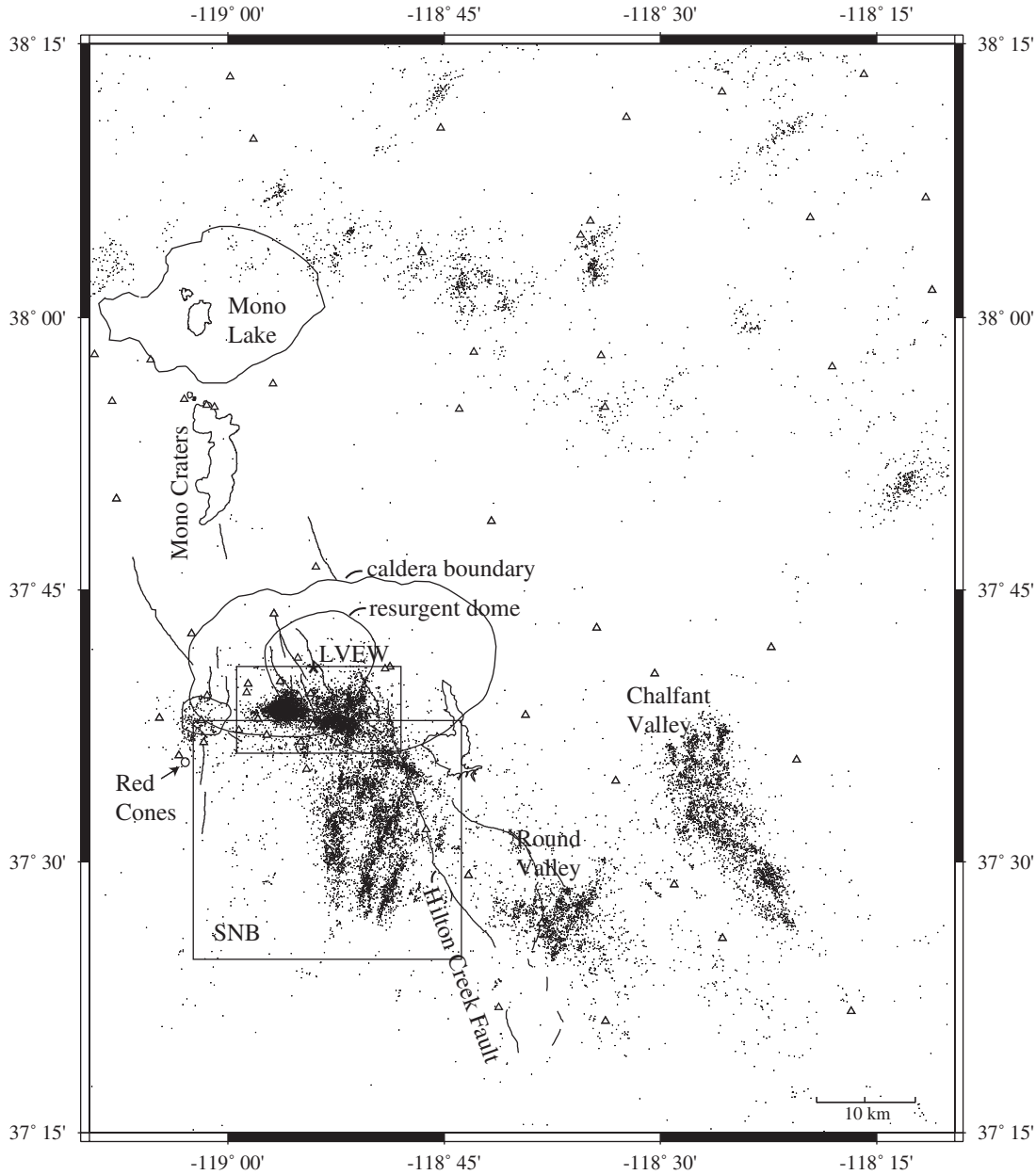

Figure 2. All earthquakes $\geq$ **M**2 in the greater Long Valley area between 1980 and 2000. Boxes show area of earthquake relocations presented in this paper. Small box is area shown in Figures 4 and 5. Large box is the area of Figure 7. Black lines denote fault traces. Triangles denote stations used to locate earthquakes (short-period seismometers) using data from the NCEDC. Star shows location of LVEW borehole seismometer.

knowledge of the stress field, we can accurately describe motion along faults with respect to one another, yielding insight into the kinematics of this complex system. Based on this analysis, we suggest a simple, tectonically driven explanation for the observed stress perturbation in the south moat of the caldera.

2. Earthquake Relocation

[5] We relocated ~45,000 earthquakes that occurred between 1980 and August 2000 in the greater Long Valley area, using the double-difference earthquake location algorithm of *Waldhauser and Ellsworth* [2000] and routinely determined arrival time readings obtained from the Northern California Earthquake Data Center (NCEDC) (Figure 2). The double-difference algorithm minimizes the residuals between observed and calculated travel time differences for pairs of earthquakes at common stations by iteratively adjusting the vector difference between the hypocenters. Thus, the double-difference method minimizes effects of unknown Earth structure without the need for station corrections. The double-difference algorithm has been shown to

Table 1. Velocity Model

Depth (km) to top of layer	P velocity (km/s)	Depth (km) to top of layer	P velocity (km/s)
0.0	3.55	7.0	6.02
0.5	3.57	10.0	6.07
1.0	3.70	14.0	6.10
2.0	5.35	18.0	6.18
3.0	5.67	30.0	6.67
5.0	5.90	50.0	8.00

produce sharp images of fault structure along the Hayward fault [*Waldhauser and Ellsworth*, 2002] and the Calaveras fault [*Schaff et al.*, 2002].

[6] We relocated earthquakes using P phase travel time differences for pairs of earthquakes separated by less than 4 km distance and the one dimensional velocity model shown in Table 1. S phase arrival times were generally not available from the NCEDC. Travel time differences were weighted based on the quality of the arrival time picks assigned by the NCEDC. Figure 3 shows a comparison of the 1997 south moat seismicity routinely located by the NCEDC using HYPO71 [*Lee and Lahr*, 1975] and relocated using the double-difference algorithm, hypoDD [*Waldhauser*, 2001]. The same arrival time picks were used in both cases. The double-difference locations clearly define many faults that are not discernable in the standard locations.

[7] The dense distribution of both seismicity and Northern California Seismic Network (NCSN) seismometers in the Long Valley area (Figure 2) allows us to obtain greatly improved relative locations using the double-difference method and catalog arrival times. Because station coverage is more complete in the south moat of the caldera than in the SNB to its south, locations in the SNB have relatively high location errors (particularly in depth) as evidenced by scatter in earthquake locations about dipping faults, as shown in section 2.2 below. Based on this scatter, we estimate a conservative upper limit of relative location error of ~1 km in the SNB, assuming that all earthquakes occurred on the same plane. Based on the same assumption, the upper limit of relative location error for south moat earthquakes is ~200 m.

[8] The errors in absolute locations are comparable to those for the initial locations obtained by the NCEDC. To estimate the absolute errors, we relocated four explosions that were detonated in the south moat of the caldera in 1983 for seismic refraction experiments conducted by *Hill et al.* [1985]. Epicenter locations for these blasts found with the double-difference method were within 0.4–0.8 km of the true epicentral locations. Depths found with the double-difference method differed from the true depths by as much as 1.6 km. We believe that the epicentral errors found for the blasts are good estimates of the absolute epicentral errors of our locations overall. However, the depth errors associated with these blasts may be higher than depth errors of relocated seismicity due to problems associated with locating events on the Earth's surface. Thus, this depth error is a conservative estimate. The errors in absolute location are consistent for all of the relocated seismicity, however. To test the robustness of the relative locations to absolute depth errors, we relocated earthquakes after shifting the initial earthquake locations by 2 km in-depth and found that the relative seismicity pattern did not change.

[9] In order to relocate the entire data set encompassing 20 years of seismicity in the Long Valley area, we broke the data into spatial and temporal subsets and relocated each subset independently. Seismicity in the south moat of the caldera was divided into five temporal subsets. Seismicity in the SNB was divided into two spatial subsets (north and south of 37.53°N or 37°32′N). We selected a group of master events and included them in each subset to observe variations in their location. The master event locations were consistent within ~200 m for all relocated subsets.

[10] In this paper we present locations of earthquakes of **M**1 and greater in the south moat of the caldera and **M**2.5 and greater in the SNB because relocated data sets with these magnitude limits had the smallest location errors. Seismicity patterns do not change when earthquakes with smaller magnitudes are included in the relocations. Although we have also relocated seismicity in Round Valley and use the resulting hypocenters in a focal mechanism stress inversion

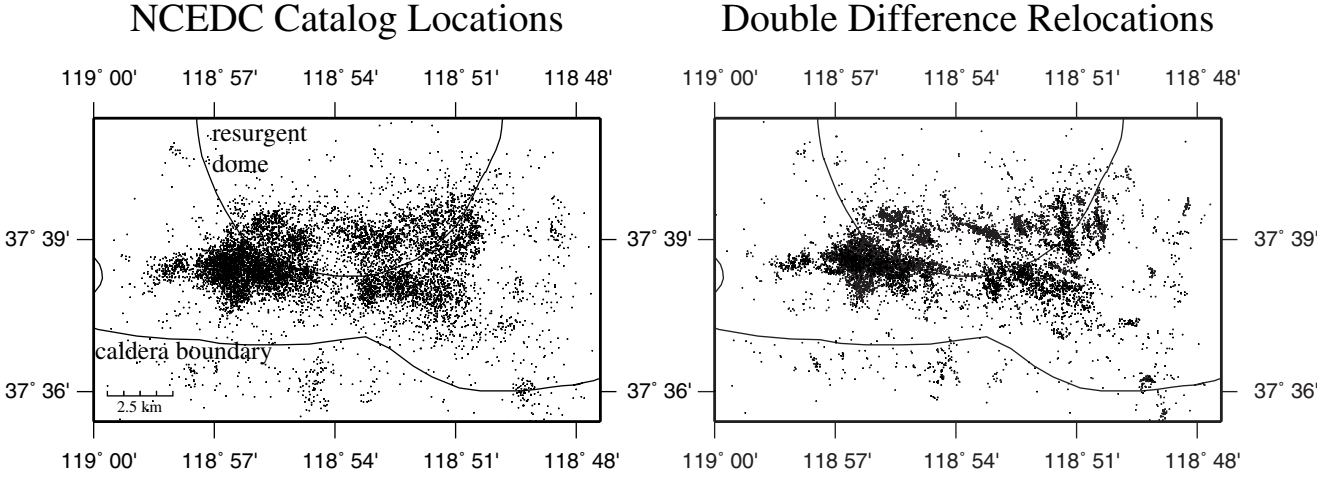

Figure 3. July 1997 to January 1998 Long Valley caldera seismicity before (left) and after (right) double-difference relocation [*Waldhauser and Ellsworth*, 2000] using P-phase catalog arrival times obtained by the NCEDC.

analysis described below, we do not specifically discuss them.

[11] Below we describe in some detail the family of faults revealed by our locations. We identified faults where clusters of earthquake hypocenters clearly form a plane in three dimensions. To determine the orientations of the faults, we fit planes to the clusters of earthquake hypocenters using least squares. The faults described in this paper are the most seismically active faults in the Long Valley area. It is likely that many other faults are currently active in the caldera area as well, but do not define seismically active planes.

2.1. South Moat and Resurgent Dome Seismicity

[12] The south moat and southern resurgent dome of the caldera have comprised an area of high seismicity since 1980. The relocated epicenters are shown in Figure 4 in 2 year "snapshots." Figure 4 illustrates that seismicity has largely occurred on the same set of faults since 1980 and that these structures have been activated in discrete temporal bursts of seismicity, or seismic swarms. In some cases, temporal propagation of seismicity within individual swarms is observed along the length or width of a fault [*Prejean*, 2002]. Seismicity in late 1997 was particularly intense and well recorded. Figure 5 shows the orientations of south moat faults based on seismicity during this time period. The major resolvable structures are summarized in Figure 6 and Table 2 and discussed further below.

[13] The largest seismic moment release in the caldera has occurred in the western portion of the south moat. We refer to this region as the western lobe of the south moat seismic zone (WSMSZ) following the work of *Hill et al.* [2002]. The WSMSZ is dominated by WSMSZ1, a fault zone oriented N72°W/80°NE which is the southern most active structure within the caldera (Figures 5 and 6) and may be related to the caldera ring fracture system [*Bailey*, 1989]. Seismic swarms have occurred repeatedly in this fault zone since 1980 (Figure 4). Unlike most of the other faults we have identified in the caldera, seismicity in this fault zone does not lie along a simple plane. Rather WSMSZ1 is a 1 km wide fault zone. We verified that this fault zone width is not an artifact of location error by observing travel time differences to the borehole seismometer in the Long Valley Exploratory Well (LVEW) (Figure 2) for earthquakes whose locations span the width of the fault zone. Focal mechanisms indicate that WSMSZ1 is composed of a series of many small faults of varying orientations.

[14] Subparallel to the WSMSZ1 fault zone, there are at least three smaller faults in the WSMSZ and the southwestern resurgent dome (SWRD) (following the work of *Hill et al.* [2002]), which have been active in each of the major seismic episodes in the caldera (1980, 1982/1983, 1990/1991, and 1997/1998) (Figure 4). These include faults WSMSZ2 and SWRD1 (southwestern resurgent dome 1), although these faults are active over a smaller depth range (6.5–8 km depth) than WSMSZ1 (3–9 km depth) and dip more shallowly to the NE (~50°) than WSMSZ1 (Figure 5, A–A′).

[15] Seismicity in the south moat continues into the eastern lobe of the south moat seismic zone (ESMSZ) across an apparent 2 km seismic gap in the central south moat. Like the WSMSZ, the ESMSZ is comprised of at least two subparallel faults striking N66°W and dipping roughly 70°N (faults ESMSZ1 and ESMSZ2) (Figure 5, B–B′). The distribution of seismic moment release indicates that this eastern extension of the fault zone is much less active than its western counterpart (Figure 5).

[16] Faults WSMSZ1 and ESMSZ1 form the southern border of seismicity in the south moat of the caldera, but north of these, relocated hypocenters define many smaller, more northerly striking faults in the southern resurgent dome. A more complex fabric of faults is visible in the southeastern resurgent dome (SERD) than in the SWRD (Figures 5 and 6). A major fault in this area is SERD1 (southeastern resurgent dome 1), which is a near vertical fault striking N60°W. North of fault SERD1, fault orientations rotate to a more N-S orientation (SERD2, SERD3, and SERD4) (Figure 6).

[17] The western and eastern lobes of the south moat seismic zone dominate each seismic episode in the south moat, but there is no evidence for surface rupture of the major E-W trending faults in these fault zones (D. Hill, personal communication, 2001), presumably because they are covered with a thick layer of poorly consolidated sediments interlayered with lava flows. However, many of the smaller, more northerly striking faults in the south moat and southern resurgent dome of the caldera show roughly the same orientation as mapped surface faults (Figure 6) [*Bailey*, 1989]. Specifically, the faults in the SE resurgent dome and fault SWRD2 may be related to the resurgent dome's medial graben or the northern extension of the Hilton Creek fault, which splinters into multiple segments within the caldera [*Bailey*, 1989].

2.2. Sierra Nevada Seismicity

[18] Figure 7 shows our relocations of seismicity in the SNB, south of the caldera, while Figure 6 and Table 2 summarize the major features. Recent seismicity south of the caldera has occurred exclusively in the footwall of the east-dipping Sierra Nevada range bounding fault, the Hilton Creek normal fault (Figure 6). The Hilton Creek fault has been essentially aseismic since 1980, yet large offsets in the glacial moraines across the fault indicate that the Hilton Creek fault has been the most active fault in the SNB region directly south of the caldera in Holocene time [*Clark and Gillespie*, 1981]. Our earthquake locations indicate that within the footwall of the Hilton Creek fault, the maximum depth of the seismogenic zone in the SNB increases toward the east (Figure 7, F–F′). There are four primary faults in this region and many minor faults.

[19] Fault SNB1, which forms the western boundary of seismicity, is a north-striking, east-dipping fault (Figure 7, D–D′) whose dip shallows slightly toward the north and possibly with depth. Faults SNB2 (N28°E/~90) and SNB3 (N28°E/~90) are two subvertical faults (Figures 6 and 7, E–E′). However, like SNB1, SNB2 and SNB3 may not be simple planes. Figure 7 shows that SNB2 may actually be composed of two parallel structures (map view), while SNB3 may be a pair of echelon planes rather than one continuous plane with depth (E–E′). Background seismicity in the SNB occurs predominately on small vertical planes parallel to SNB2 and SNB3, the easternmost of which are visible in Figure 7, but small cross planes also exist in the area. These minor planes are too poorly defined by seis-

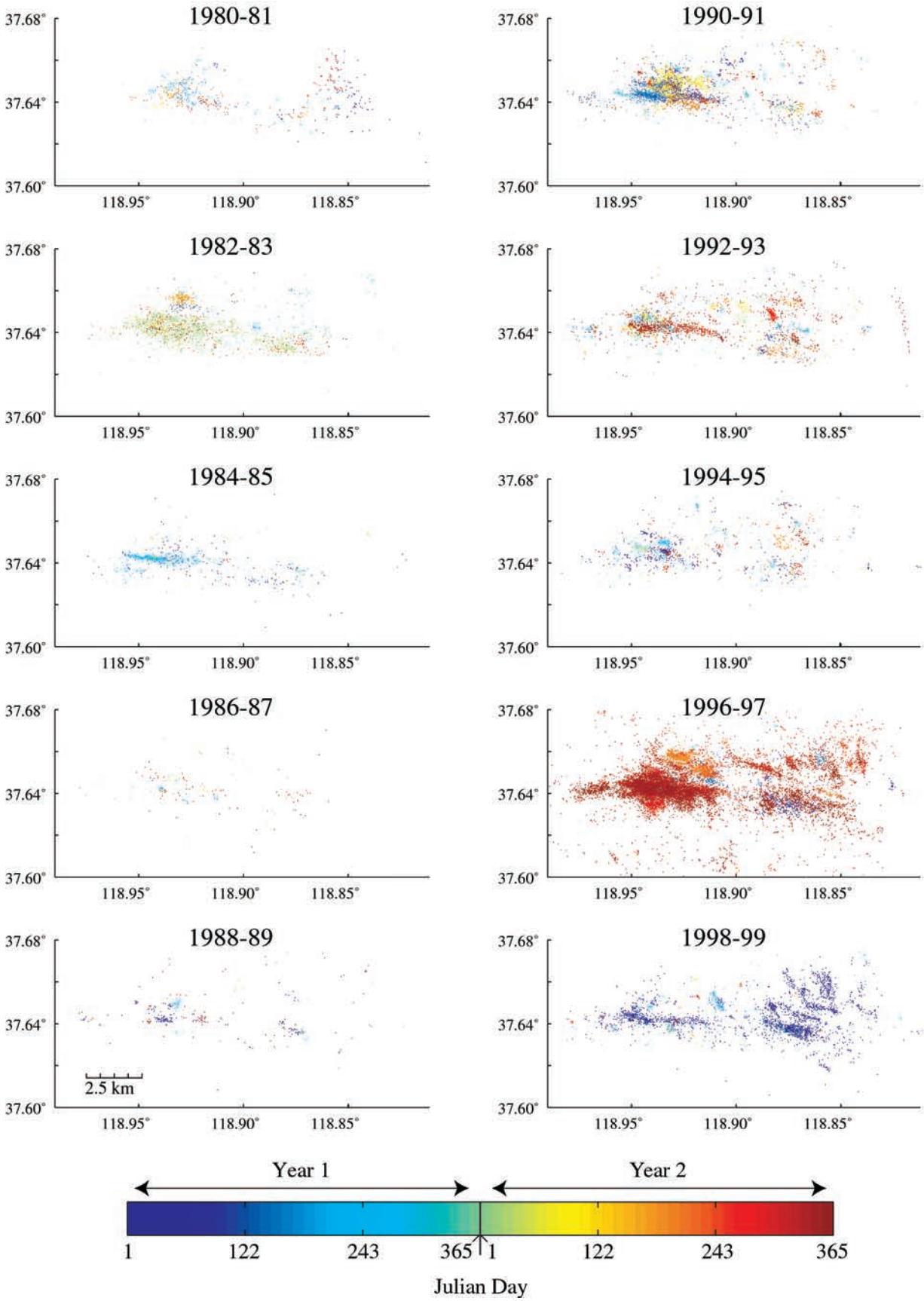

Figure 4. Epicenters of relocated > **M**1 earthquakes in the Long Valley caldera between 1980 and 2000 in 2 year time spans, colored with time. Note that the catalog was not complete at **M**1 until at least 1983. Area of plot shown in Figure 2.

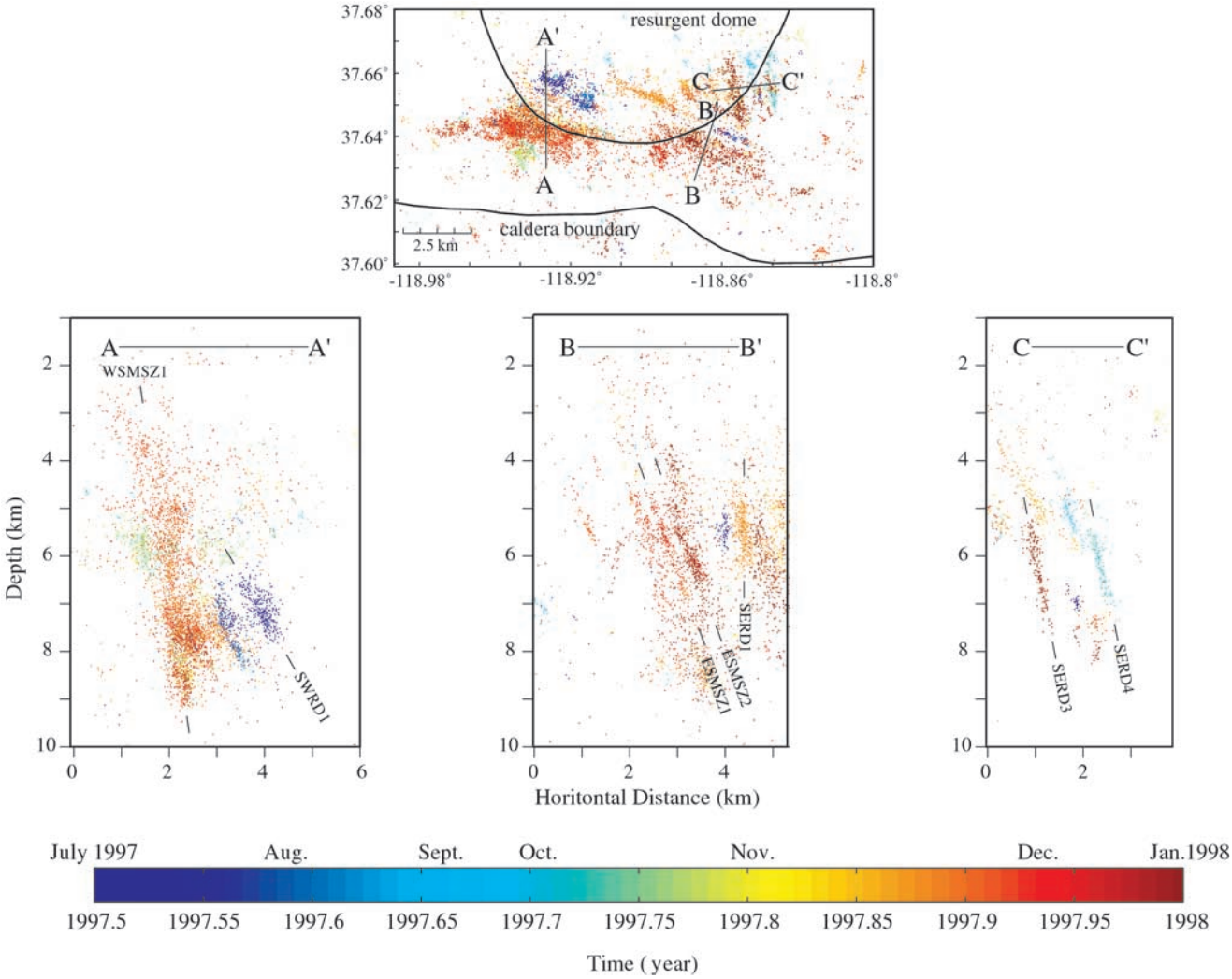

Figure 5. Relocated hypocenters of July 1997 to January 1998 Long Valley caldera seismicity in map view (top) and three cross sections (bottom), colored with time. See Figure 6 for fault labels. Cross section A–A′ shows hypocenters west of −118.905. B–B′ shows hypocenters east of −118.905 along transect line shown in map view. C–C′ shows hypocenters east of −118.905 and north of 37.643 along transect line shown in map view. Area of plot shown in Figure 2.

micity to determine a robust orientation estimate. SNB4 is a N70°W/60°NE feature that generally lies along the same trend as the south moat faults WSMSZ1 and ESMSZ1. Although SNB4 may have slipped in the **M**6 1980 earthquake sequence, this fault was otherwise seismically quiet until 1997.

2.3. M5+ Earthquakes in the Long Valley Area, 1980–2000

[20] Figure 8 and Table 3 give the double-difference locations for all earthquakes with **M**5 or greater in the Long Valley area since 1980, numbered chronologically. In order to better understand these events, we have attempted to identify the fault planes that accommodated slip in these earthquakes based on their locations and focal plane solutions. Most of the **M**5+ events are located on one of the faults defined by seismicity. In these cases, we assume that the nearby faults were the earthquakes' rupture planes (Table 3) if predominantly double-couple focal plane solutions support this assumption. The focal plane solutions for earthquakes that have well-defined first motion mechanisms or that have complete moment tensor solutions are shown in Figure 8. In the cases in which the earthquakes are not located along known faults, we have not listed the associated planes in Table 3.

[21] Even though the focal mechanisms for the 1980 **M**6 earthquakes (events 1, 3, and 8) are debated and may be non-double-couple events [*Given et al.*, 1982; *Wallace et al.*, 1982; *Julian and Sipkin*, 1985; *Wallace*, 1985], we attempt to associate these earthquakes with known fault planes. The non-double-couple nature of these earthquakes could result from simultaneous slip on multiple rupture planes as suggested by *Ekström* [1983] or simultaneous shear slip and magmatically driven fluid injection as suggested by *Julian and Sipkin* [1985]. If the non-double-couple nature of these moment tensors results from complex slip on multiple rupture planes, the focal mechanism for earthquake 1 may be caused by near-simultaneous strike-

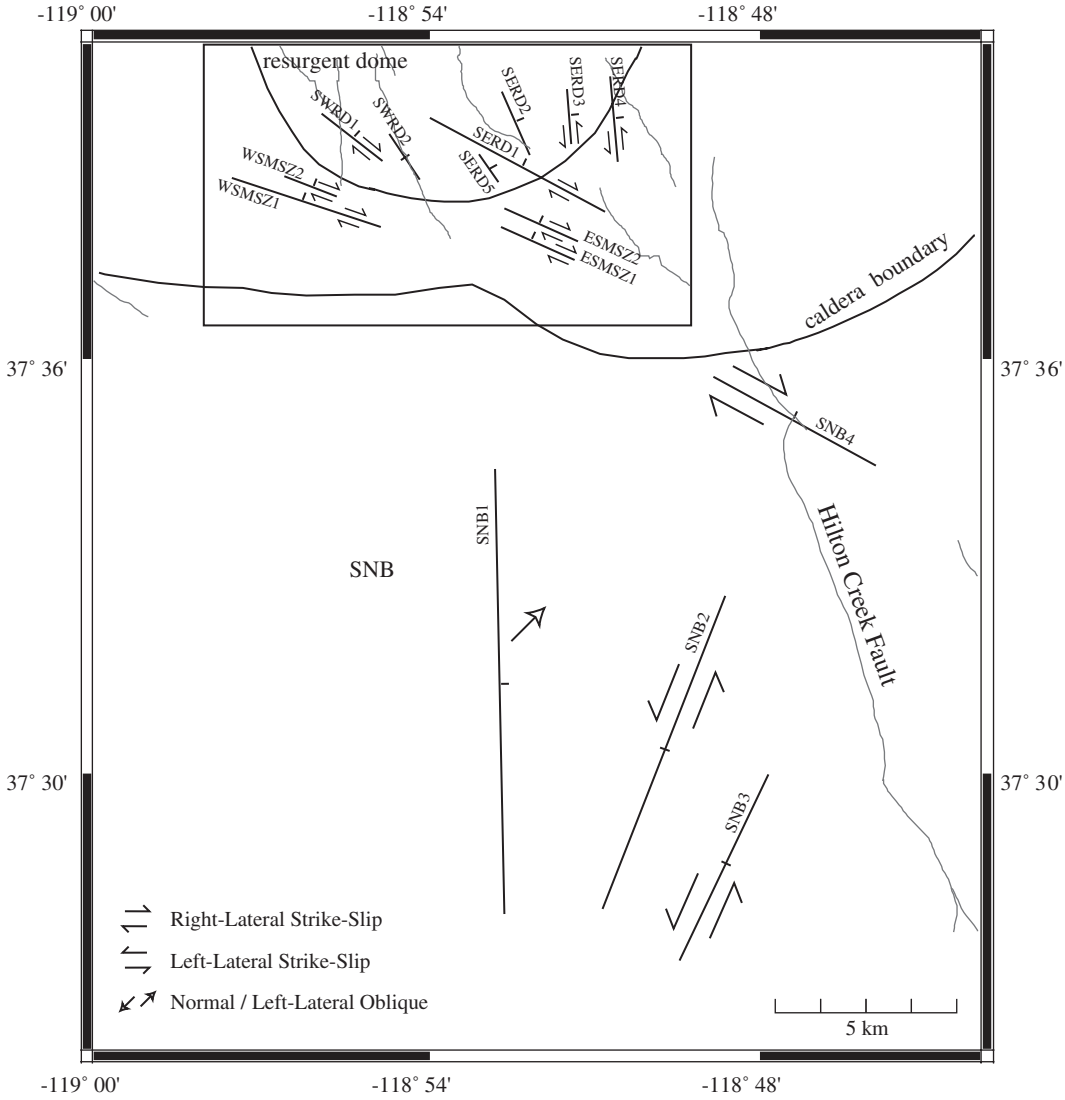

Figure 6. Map of faults identified by relocated recent seismicity in the Long Valley caldera and in the Sierra Nevada basement south of the caldera. Faults are named based on their location, where WSMSZ = western lobe of the south moat seismic zone, ESMSZ = eastern lobe of the south moat seismic zone, SERD = southeastern resurgent dome area, SWRD = southwestern resurgent dome area, and SNB = Sierra Nevada block. Arrows show the relative sense of slip on the faults. Thin lines are mapped surface traces of faults [*Bailey*, 1989].

slip motion on plane SNB4 and normal motion on a fault SNB1. These fault geometries and slip distributions are similar to those that *Ekström* [1983] found best explained waveforms for this event. Similarly, the mechanism for earthquake 8 may result from near-simultaneous strike-slip motion on SNB3 and a normal motion on fault SNB1. Because this appears to be a strike-slip/normal faulting stress regime in which Sh_{MAX} (maximum horizontal stress) $\sim S_V$ (vertical stress) (see section 4.1 below), this slip configuration seems reasonable if the earthquakes nucleated at depth and ruptured simultaneously upward along two planes, particularly because earthquakes 1 and 8 both produced aftershocks on fault SNB1.

[22] Since 1980, the SNB faults shown in Figure 6 and the WSMSZ and ESMSZ have probably all ruptured in moderate-sized earthquakes, but uncertainties in the slip distribution of the 1980 earthquakes makes it impossible to state this with certainty. We suggest that seismic slip is distributed throughout this region, as the microseismicity suggests. It is interesting to note that the **M**6 1980 earthquake 2 nucleated in the gap between the WSMSZ and the ESMSZ.

3. Focal Mechanism Stress Inversions

[23] To constrain the stresses driving slip on faults in the Long Valley area, we performed focal mechanism stress inversions using first motion focal mechanisms obtained from the NCEDC. The NCEDC determines focal mechanisms using FPFIT [*Reasenberg and Oppenheimer*, 1985]. We used the methods of both *Gephart and Forsythe* [1984] and *Michael* [1987] to infer principal stress directions from

Table 2. Faults in the Long Valley Area and Their Sense of Slip

Fault	Longitude	Latitude	Depth (km)	Strike	Dip	Width (km)	Length (km)	Rake 1[a]	S.D.	Rake 2[b]	Region
SNB1	−118.8712	37.5198	6.5	359	64	7	12	−45	30	−33	D2
SNB2	−118.8291	37.5052	6	21	90	6	9	2	45	−15	D3
SNB3	−118.811	37.4774	6	26	90	10	5.6	7	28	−5	E3
SNB4	−118.785	37.5919	7.5	298	60	3.5	5	178	38	−159	C3
SERD1	−118.8729	37.6475	5.5	298	84	2	5.3	–	–	−174	B2
SERD2	−118.8712	37.6576	4.8	336	70	1.6	1.84	–	–	−115	B2
SERD3	−118.8558	37.6584	6	355	80	2	1.5	−2	29	−45	B2
SERD4	−118.8406	37.658	6.3	354	75	2.6	2.3	−20	27	−59	B2
SERD5	−118.8804	37.6469	8	326	70	1	1	–	–	−135	B2
ESMSZ1	−118.8639	37.6337	7	294	70	4.4	2.3	179	24	−165	B2
ESMSZ2	−118.8648	37.6347	6	294	73	2.1	2.3	176	19	−167	B2
WSMSZ1	−118.9354	37.6422	6	288	80	6.1	4.2	NA	–	−168	B1
WSMSZ2	−118.9331	37.6475	7.6	326	70	1.1	1	NA	–	−96	B1
SWRD1	−118.921	37.6559	7.5	307	70	2.1	2.1	–	–	−138	B1
SWRD2	−118.9077	37.6487	8	327	90	2	1.5	–	–	−180	B1

[a] Method 1: rake averaged from focal mechanisms, not enough data (–), not a simple fault plane (NA).
[b] Method 2: rake calculated based on stress model.

the focal mechanisms. We selected these two methods because they are well tested and commonly used.

[24] Focal mechanism stress algorithms are based upon the premise that faults slip in the direction of maximum resolved shear traction on the fault plane. Constraining the stress field using earthquake focal mechanisms and these algorithms requires three assumptions as follows (see the work of *Gephart* [1990a] for discussion). (1) The focal mechanisms are accurate representations of the earthquake source. (2) Stresses are homogeneous in the volume containing the selected focal mechanisms. (3) The focal mechanisms represent a variety of faulting orientations, because one cannot deduce reliable stress orientations from either a single focal mechanism or an arbitrary number of similar focal mechanisms [e.g., *McKenzie*, 1969].

[25] In attempt to satisfy the first assumption, we invert only those focal mechanisms that we consider to be of high quality with relatively little error in nodal plane orientations. We select focal mechanisms that are constrained by at least 50 first motions and have unique solutions. To minimize problems associated with the second assumption, we limit areas of the inversions to a 5 × 5 km horizontal grid (Figure 9). Finally, in attempt to satisfy assumption 3, we only inverted gridded intervals (shown in Figure 9) which encompassed at least 30 earthquakes between 1980 and 2000. Figure 9 shows the areas for which we inverted for stress, the epicenters of the earthquakes used in the inversions, stereographs of the corresponding P and T strain axes for the focal mechanisms, and stereographs of the confidence intervals of our results. Figure 10 shows directions of T strain axes from focal mechanisms in the Long Valley area to illustrate how the data vary spatially over the region.

[26] We find that the *Gephart and Forsythe* [1984] method and the *Michael* [1987] method give results that generally agree, although the uncertainties reported by each method differ (see the work of *Hardebeck and Hauksson* [2001] for discussion of errors). Because the uncertainties estimated by the *Gephart and Forsythe* [1984] method are greater than the uncertainties estimated by the *Michael* [1987] method (and because we prefer to possibly overestimate uncertainties rather than underestimate them), we present only the results of the *Gephart and Forsythe* [1984] method in Table 4. We find that calculated R values ($R = (S_2 - S_1)/(S_3 - S_1)$, where S_1, S_2, and S_3 are the principal stresses) tend to be highly variable in adjacent regions. R values vary between R = 0 and R = 0.7. A bootstrap analysis reveals that the principal stress direction results are robust, though results for R values are not well constrained by the data. This can arise when small errors in the orientation of the nodal plane lead to large differences in R [*Angelier*, 1979]. Therefore, we conclude that R values are poorly resolved and insufficiently reliable to be used in subsequent analysis.

[27] Figure 11 shows the minimum horizontal stress directions (Sh_{MIN}) obtained from the inversions combined with results from other stress indicators. The E-W relative extension in the Round Valley area, SE of Long Valley, and the NW–SE relative extension direction in the Long Valley caldera west moat and Mammoth Mountain areas are consistent with the regional Sh_{MIN} direction characteristic of the Walker Lane zone on the western edge of the Basin and Range province which was determined based on fault offset and earthquake focal mechanism analyses [*Bellier and Zoback*, 1995]. The E-W Sh_{MIN} direction implied by opening of the N-S trending Mono/Inyo dike [*Bursik and Sieh*, 1989] is also generally consistent with this regional stress field. However, we find that within the caldera, the Sh_{MIN} direction is locally perturbed to NE–SW relative extension, verifying the results of *Moos and Zoback* [1993] (Figure 11 and Table 4). This perturbation gradually rotates to the regional Sh_{MIN} direction with distance south of the caldera. Although focal mechanism data are too sparse for a formal stress inversion immediately north and SW of the Long Valley caldera, P/T axes from the earthquakes focal mechanisms in these areas imply E-W to NW–SE relative extension, consistent with the background stress field. This implies that the stress perturbation is centered roughly in the south moat/southern resurgent dome area.

[28] The average misfit values for these inversions are large considering the large number of first motions used to constrain the focal mechanisms (Table 4). This probably results from a combination of the spatially varying stress field and errors in the focal mechanisms. If the stress field varies within the 5 × 5 km bins, we are not satisfying the assumption that the stress field is homogeneous within each inverted volume. However, if we decrease the bin size, we

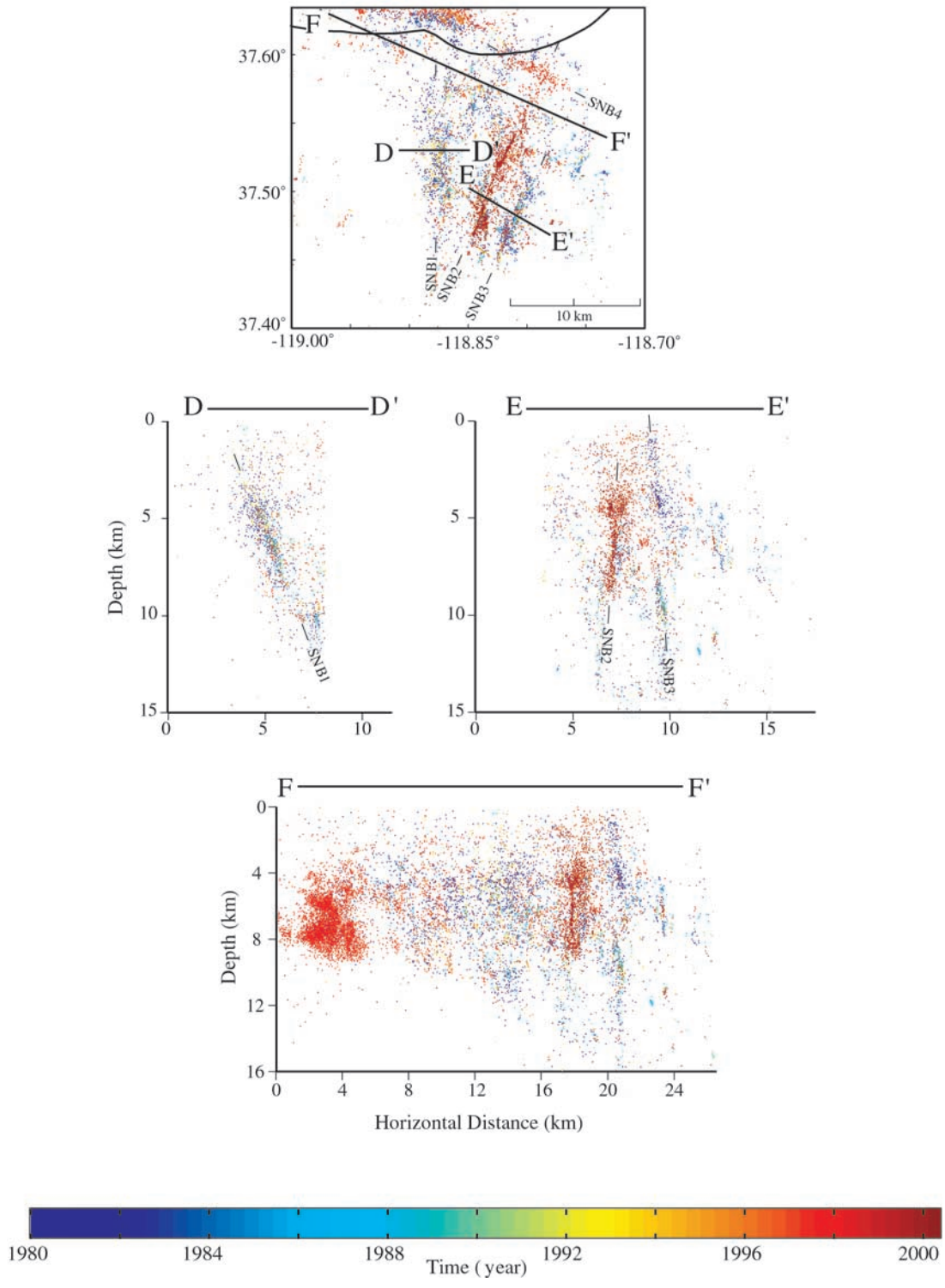

Figure 7. Relocations of > **M**2.5 earthquakes in the SNB between 1980 and August 2000 in map view (top) and three cross sections (bottom), colored with time. See Figure 6 for fault labels. Cross section D–D′ shows hypocenters south of 37.55 and west of −118.85. E–E′ shows hypocenters south of 37.57 and east of −118.85. F–F′ shows all relocated hypocenters. Area of plot shown in Figure 2.

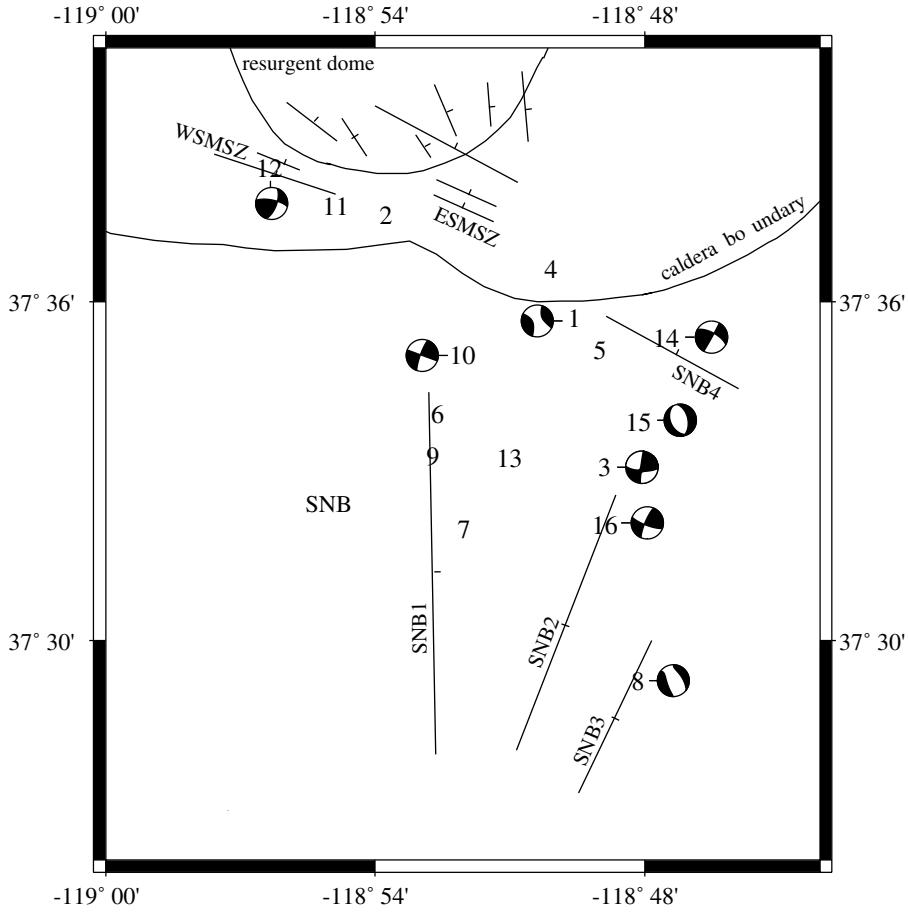

Figure 8. Map of relocated epicenters for all earthquakes $\geq$ **M**5 in the Long Valley area, 1980–2000, numbered chronologically. Focal plane solutions for the well-constrained events are next to the numbered locations. In the cases where no focal mechanism is shown, either a focal mechanism has not been determined for the event or the focal mechanism is poorly constrained. Sources of focal plane solutions: numbers 1, 3, and 8: *Julian and Sipkin* [1985]; numbers 10 and 12: NCEDC; and numbers 14, 15, and 16: University of California-Berkeley Seismological Laboratory.

will greatly reduce the number of active faults in each bin, leading to insufficient fault diversity and poorly constrained results. The second cause of the large misfits is errors in the focal mechanisms themselves. Although these events have a large number of first motions, in some cases the nodal planes are poorly constrained due to erroneous polarity readings and a lack of data in crucial areas of the focal sphere. However, despite the large misfits, we have con-

Table 3. **M**5+ Long Valley Region Earthquakes, 1980–2000

	Date	Time	**M**	Latitude	Longitude	Depth	Associated planes
1[a]	25 May 1980	1633	6.10	37.59524	−118.82621	8.214	SNB4
2	25 May 1980	1649	6.00	37.62577	−118.89601	4.833	WSMSZ/ESMSZ
3[a]	25 May 1980	1944	6.10	37.55127	−118.81492	12.866	SNB2
4	25 May 1980	2035	5.70	37.60962	−118.83481	4.627	–
5	25 May 1980	2059	5.00	37.58573	−118.81657	7.642	–
6	26 May 1980	1224	5.10	37.56686	−118.87672	7.035	SNB1
7	26 May 1980	1857	5.70	37.53278	−118.86699	6.773	SNB1
8[a]	27 May 1980	1450	6.20	37.48816	−118.80260	14.380	SNB3
9	1 August 1980	1638	5.40	37.55440	−118.87867	7.287	SNB1
10[a]	30 September 1981	1153	5.90	37.58434	−118.86764	6.410	–
11	7 January 1983	0138	5.40	37.62841	−118.91474	4.365	WSMSZ
12[a]	7 January 1983	0324	5.30	37.63956	−118.93922	7.153	WSMSZ
13	3 July 1983	1840	5.30	37.55373	−118.85021	11.095	SNB1
14[a]	9 June 1998	0524	5.13	37.58946	−118.79198	8.252	SNB4
15[a]	15 July 1998	0453	5.11	37.56453	−118.80235	7.604	–
16[a]	15 May 1999	1322	5.60	37.53404	−118.81471	7.062	SNB2

[a] Events with well-constrained focal mechanisms shown in Figure 8.

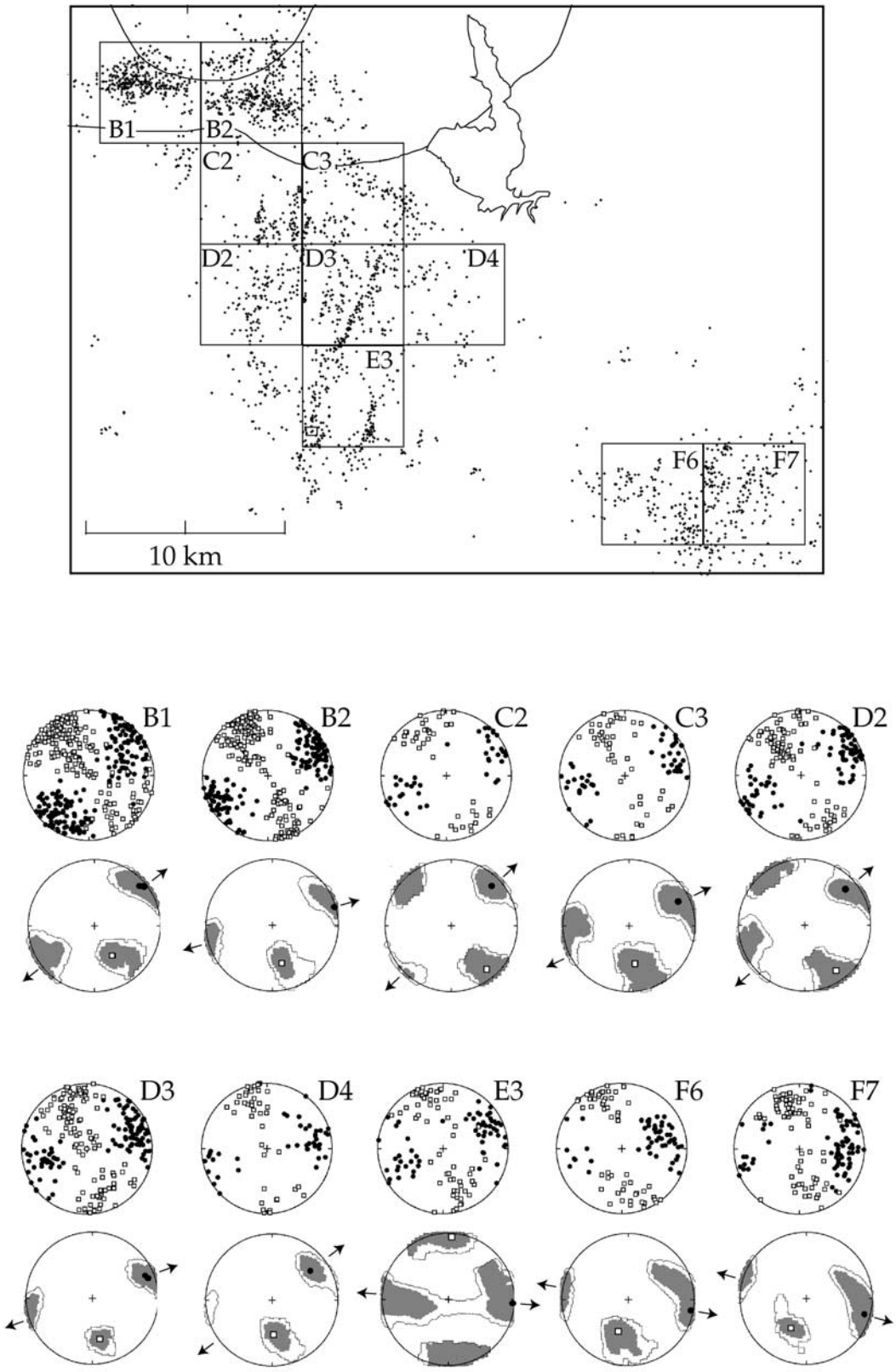

Figure 9. Map of earthquakes used in focal mechanism stress inversions using FMSI [*Gephart*, 1990b]. Inverted regions are shown in numbered boxes. For each box, P/T axes of the inverted earthquakes are shown in lower hemisphere projections (T axes = black circles and P axes = white squares) with the corresponding stress axes results shown below the P/T plots (S3 = black circle and S1 = white square). The 68% (shaded) and 95% (white with black outline) confidence regions are shown. Stereographic plots were constructed using FMSI software [*Gephart*, 1990b].

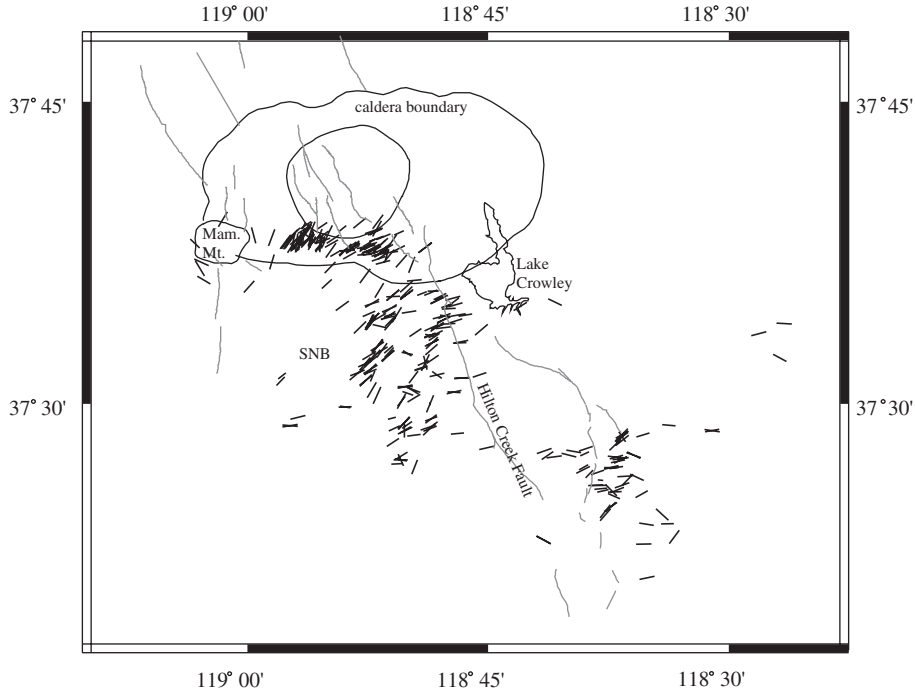

Figure 10. Azimuth of T axes for all earthquakes with more than 75 first motion readings. Gray lines denote fault traces.

fidence that the observed stress rotation is real since it is quite evident in the spatial variations of T axes (Figure 10).

4. Synthesis and Discussion

4.1. Fault Kinematics of the Long Valley Area

[29] By combining fault orientations obtained from relocated seismicity with knowledge of the motion across the faults, we can determine slip vectors on the fault planes and generate a model of fault motions in the caldera and SNB. We calculate average slip vectors in two ways. We average the rakes on the fault planes based on focal mechanisms (method 1), and we calculate slip vectors on fault planes (determined from the relocated seismicity) using stress results from the focal mechanism inversions and an assumed R value, as explained below (method 2).

[30] To estimate the average rake on each fault plane using focal mechanisms directly (method 1), we select all focal mechanisms that are located within 200 m of a given fault plane. For many of these, one of the nodal planes coincides with the measured fault plane within ±25°. If the disagreement is greater than 25°, we assume that the earthquake is not occurring on the fault plane or that the focal mechanism is not well constrained and remove it from the data set. The rakes on the presumed fault plane are then averaged to obtain an average rake (Rake 1 in Table 2).

[31] As an example of method 1, Figure 12 shows focal spheres with compression and dilatation readings and the corresponding focal plane solutions for plane SERD4 [*Reasenberg and Oppenheimer*, 1985]. We selected this fault as an example because the limited amount of data permits us to show all of the focal mechanisms used in this study. In eight out of nine cases, the fault defined by microseismicity (dashed line) is either consistent with one of the nodal planes of the focal mechanism solution (a–d) or is generally consistent with constraints provided by the compression and dilatation measurements (e–h). This implies that many of the earthquakes with focal mechanisms, which do not correspond well with the relocation defined fault plane, are poorly determined and are not actually rupturing a different plane. This example also demonstrates the reliability of rake method 1 for determining fault motions.

[32] To calculate rakes on the fault planes using method 2, we must know the orientations of the principal stresses and their relative magnitudes. We obtain the orientations of the principal stresses from the focal mechanism stress inversion analysis described previously. Because the R values from the stress inversions are poorly constrained, we use information about the tectonic environment to establish the relative magnitudes of the stresses to complete our stress model. Because analyses of earthquake focal mechanisms, fault offsets, borehole breakouts, hydraulic fracturing, and the alignment of young volcanic vents indicate that this is a normal faulting/strike-slip faulting regime [*Zoback*, 1989; *Moos and Zoback*, 1993; *Bellier and*

Table 4. Focal Mechanism Stress Inversion Results

Grid interval	S1 az	S1 pl	S2 az	S2 pl	S3 az	S3 pl	Misfit
B1	148	45	315	45	52	6	14.9
B2	165	40	342	50	74	2	12.8
C2	141	15	272	68	46	16	10.1
C3	170	41	316	44	64	18	11
D2	145	16	272	64	49	19	12
D3	168	37	326	51	70	11	10
D4	176	46	304	31	53	28	8.7
E3	4	7	198	83	94	2	14
F6	195	48	6	42	100	4	9.9
F7	206	48	8	41	106	9	11.8

S1, S2, and S3 are the maximum, intermediate, and minimum principal stresses, respectively, az is azimuth, and pl is plunge.

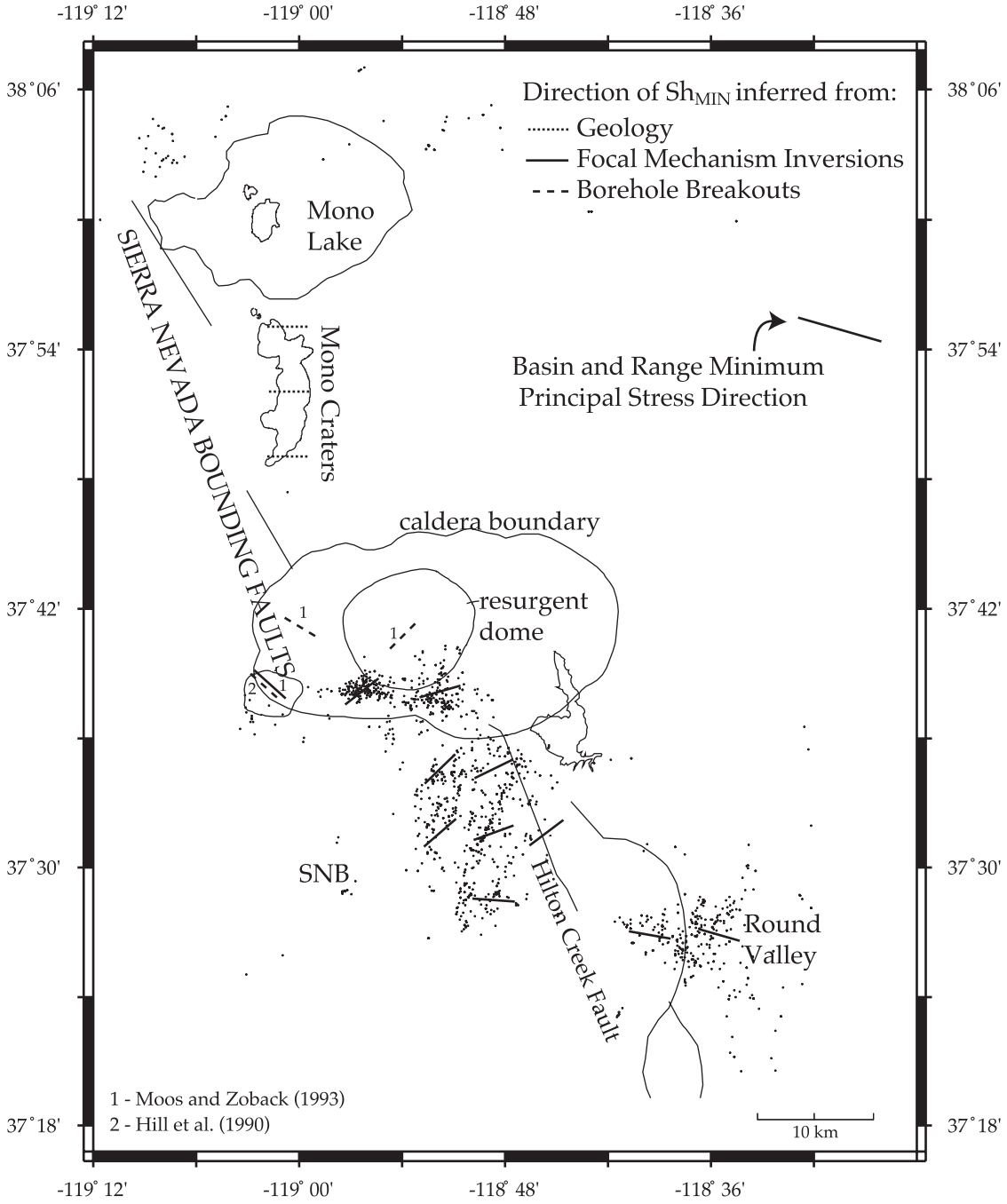

Figure 11. Map showing trajectories of Sh_{MIN} in the Long Valley area based on focal mechanism stress inversions (this work) (solid lines), borehole breakouts (1) [*Moos and Zoback*, 1993] and T axes (2) [*Hill et al.*, 1990] (dashed lines), and geological indicators [*Bursik and Sieh*, 1989] (dotted lines). Dots are epicenters of earthquakes used in stress inversions.

Zoback, 1995], we assume that the maximum horizontal stress is roughly equal to the vertical stress and R $\sim$ 0.

[33] Table 2 demonstrates that method 1 and method 2 give results that are generally consistent for all faults with the exception of faults SERD3 and SERD4. Because method 2 predicts a greater component of normal motion than we observe on SERD3 and SERD4, the R value in the SE resurgent dome area may be higher than in other regions of the study area, for which R = 0 seems to be a good approximation. General agreement between the two methods supports the appropriateness of our stress model and justifies our use of the stress model to derive the general sense of slip on these faults. Therefore, we use the stress model to find the sense of motion on planes in the caldera for which the slip direction cannot be determined from focal mechanisms.

[34] Figure 6 demonstrates schematically how fault blocks are moving seismically in the caldera. In the western and eastern lobes of the south moat seismic zone, most of the subparallel faults trending roughly EW and dipping 70–80°NE have nearly pure right-lateral strike-slip motion.

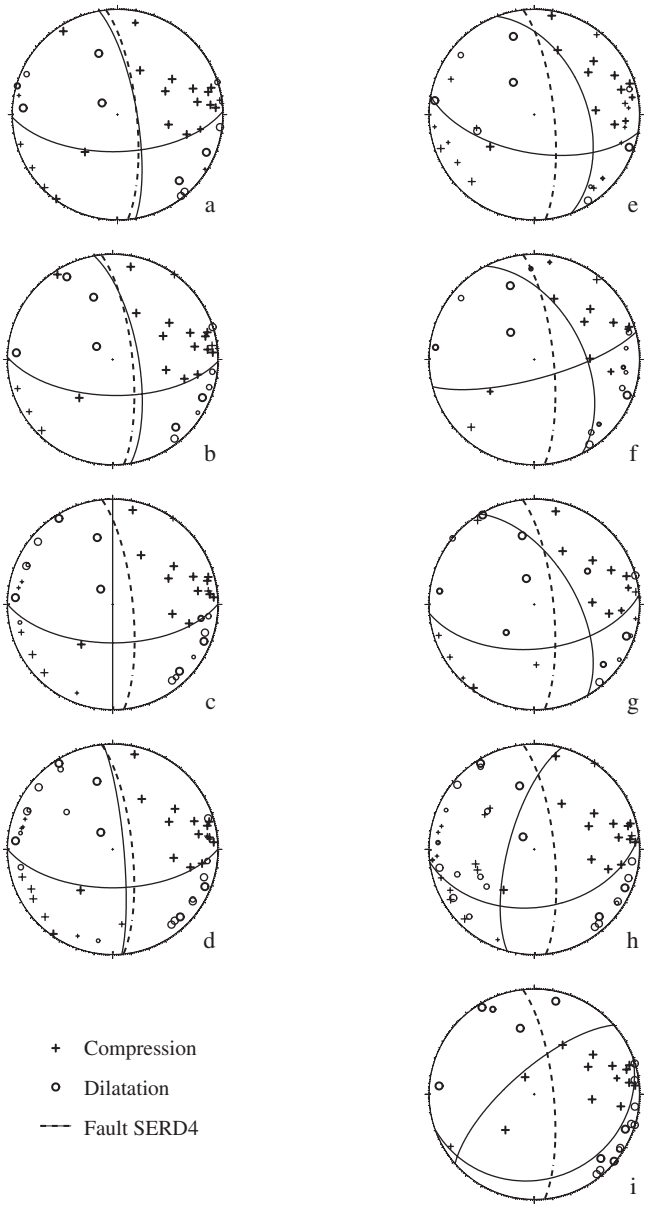

Figure 12. Focal mechanisms used in this study for earthquakes within 200 m of plane SERD4. Mechanisms in the left column agree with the identified plane (dashed line) within 25° and are therefore to obtain an average rake on the plane (Table 2). Mechanisms in the right column are not included in finding the average rake, as they do not fit the defined plane within 25°.

Thus, despite their northward fault dips, these faults are currently not acting as normal faults. Similarly, the more northerly trending, east-dipping faults in the eastern resurgent dome area are slipping in a predominantly left-lateral sense.

[35] The slip distribution on faults inside the caldera based on our slip analysis is reflected in 1997/1998 geodetic data. Deformation in 1997/1998 was dominated by inflation beneath the resurgent dome [*Simons et al.*, 2000]. However, inflation beneath the resurgent dome does not account for all of the deformation observed. The residual is best modeled by a ~east/west-striking, steeply dipping right-lateral strike-slip fault across the length of the south moat (J. Langbein, personal communication, 2002). This fault identified geodetically corresponds to faults in the west lobe and east lobe of the south moat seismic zone identified by seismicity.

[36] In the SNB, fault SNB1 is a normal fault with a left-lateral strike-slip component, while SNB2 and SNB3 are pure left-lateral strike-slip faults. If SNB1 is assumed to continue along its downdip projection to depths ~2 km deeper than the observed seismicity (Figure 7), seismicity in the SNB is confined to the hanging wall of SNB1. Because SNB1 is subparallel to the Hilton Creek fault, its activity might be thought of as the westernmost extent of Basin and Range normal faulting at this latitude.

[37] Although fault SNB4 is not directly connected to the south moat seismicity, kinematically it appears to be an extension of the south moat shear zone formed by the WSMSZ and the ESMSZ because these fault zones are aligned, have a similar orientations, and are characterized by right-lateral motion. The onset of right-lateral slip on fault SNB4 beginning in 1997 combined with right-lateral slip in the south moat and left-lateral slip on fault SNB2 have delineated a subblock of Sierra Nevada crust which appears to be escaping to the SW relative to the caldera, as described by *Hill et al.* [2002].

4.2. Evaluating Possible Sources of the South Moat Stress Perturbation

[38] We now attempt to integrate the earthquake relocation and stress inversion results to examine possible driving forces for activity in the caldera region and the interaction between tectonic and magmatic processes. To do this, we model two simple end-member scenarios using Coulomb 2.0 [*Toda et al.*, 1998] and investigate the apparent stress anomaly predicted for each in the south moat and adjacent SNB. We evaluate the likelihood of each model based on the stress inversion results shown in Figure 11. The first model, in which we calculate stresses resulting from an inflational source, represents a purely magmatically driven system. The second model, in which we calculate stresses resulting from extension across the Mono/Inyo dike chain and the Hilton Creek fault, represents a primarily tectonically driven system.

[39] In the first model, we represent magma chamber inflation beneath the resurgent dome as a Mogi point source at 10 km depth [*Simons et al.*, 2000] with 0.1 km^3 of inflation [*Battaglia et al.*, 1999]. To understand how the local stresses induced by inflation interact with the larger-scale tectonic environment, we must also estimate the background regional stress field. To do this, we use Coulomb faulting theory and assume R = 0, a coefficient of friction of 0.6 (see the work of *Townend and Zoback* [2000] for review), and that the minimum compressive stress, S_3, is horizontal and oriented N80°W [*Zoback*, 1989; *Bellier and Zoback*, 1995]. We also assume that the pore pressure is superhydrostatic (Pp = 0.8 S_V), as has been suggested for this region by *Moos and Zoback* [1993]. This leads to the following regional stress regime at 6.5 km depth (the average depth of seismicity and of the focal mechanism stress inversion measurements): S_1 (N10°E) = S_V (vertical stress) = 175 MPa, S_3 (N80°W) = 151 MPa.

[40] Figure 13 shows the calculated directions of S_3 at 6.5 km depth due to inflation of the Mogi source. In

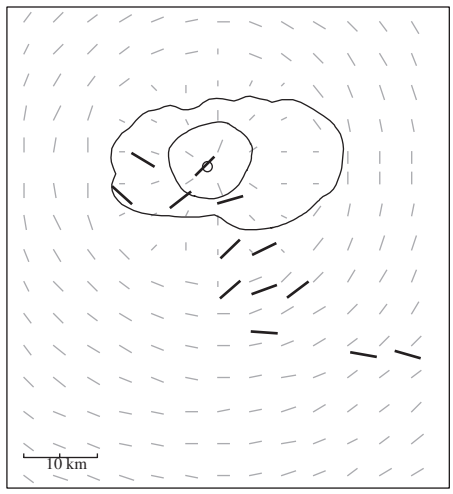

a) S_3 directions due to Mogi source, assuming isotropic stress field.

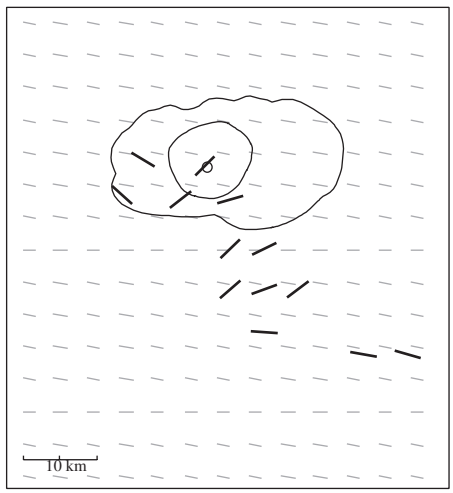

b) S_3 directions due to Mogi source (a) and realistic regional stress field.

Figure 13. Dislocation modeling results of S_3 direction due to 0.1 km^3 inflation of a Mogi source at 10 km depth (gray lines). Black lines are S_3 observations for comparison. Line length indicates plunge of S_3 axis where short lines are steeply plunging. Location of Mogi source shown with circle. (a) S_3 direction due to inflation where the only source of stress is the local inflation of the Mogi source (no deviatoric stress in the far field). (b) S_3 direction due to the inflational source (shown in (a)) combined with estimated background regional stress field calculated assuming high pore pressure ($Pp = 0.8\ S_V$).

Figure 13a the only source of stress is the local inflation of the Mogi source (no deviatoric stress in the far field). In Figure 13b the local stress due to inflation has been superimposed over the background regional stress field described above. In the case where there is no background stress field (Figure 13a), inflation creates a radially symmetric pattern in the S_3 direction about the center of resurgent dome (short lines denote steeply plunging S_3). This magmatically driven model is inconsistent with stress observations within the caldera, immediately south of the caldera, and in Round Valley (30 km SE of the caldera), although it correctly predicts the S_3 direction in the mid-SNB. Interestingly, when the stresses from the inflational source are combined with the regional background stress field, the inflation signal is too weak to significantly perturb the background stress field (Figure 13b) at the average depth of seismicity, and therefore, cannot explain the observed stress field perturbation. These conclusions do not change significantly for source depths ranging from 7 to 15 km. Thus, an inflating magma chamber beneath the resurgent dome as the sole source of the stress perturbation does not seem to be a likely hypothesis.

[41] Alternatively, regional tectonic processes could be instrumental in driving deformation in the area, resulting in the observed stress perturbation. The Long Valley caldera is located in a NW–SE elongated band that bounds the eastern Sierra Nevada and accommodates both Basin and Range WNW–ESE extension and right-lateral shear strain due to plate boundary motion between the North American and Pacific plates. Roughly 60 km SE of Long Valley in Owen's Valley, right-lateral shear is observed across the width of the NW elongated valley due to motion of the eastern California shear zone [*Savage and Lisowski*, 1995]. The eastern California shear zone appears to extend northward from Owen's Valley into the Chalfant Valley based on the occurrence of recent right-lateral strike-slip earthquakes in Chalfant Valley [*Smith and Priestley*, 1988]. Although Chalfant Valley is located less than 40 km east of Long Valley (Figure 1), it is not known if Long Valley is affected by the eastern California shear zone as well. Immediately south of the Long Valley caldera, the large normal-slip displacements in the glacial moraines on the Hilton Creek fault indicate that this fault has accommodated a large portion of regional WNW–ESE extension in Holocene time, averaging one **M**6.5 earthquake roughly every 500 years [*Clark and Gillespie*, 1981]. Because the Hilton Creek fault scarp and the earthquake focal mechanisms in the area do not show evidence of right-lateral shear across the Hilton Creek fault, we assume that the Hilton Creek fault has been unaffected by the eastern California shear zone and has been accommodating regional WNW–ESE Basin and Range extension in Holocene time.

[42] North of the caldera, the opening of the Mono/Inyo dike chain has likewise accommodated a large portion of regional WNW–ESE extension along the Sierran front [*Bursik and Sieh*, 1989]. For example, the eruption which formed Obsidian Dome ~600 years ago [*Bailey*, 1989] was fed by a dike which was 7 m thick in the EW direction [*Eichelberger et al.*, 1986]. As Figure 14 shows, the WNW–ESE trending faults in the south moat of the caldera, form a right-lateral "transform" zone in the left step over between the Hilton Creek fault and the Mono/Inyo dike. Thus, we suggest that the south moat stress perturbation may be a result of the overall geometry of the Sierran front and localized areas of tectonic extension might be providing conduits for magma and magmatically derived fluids to move to the surface.

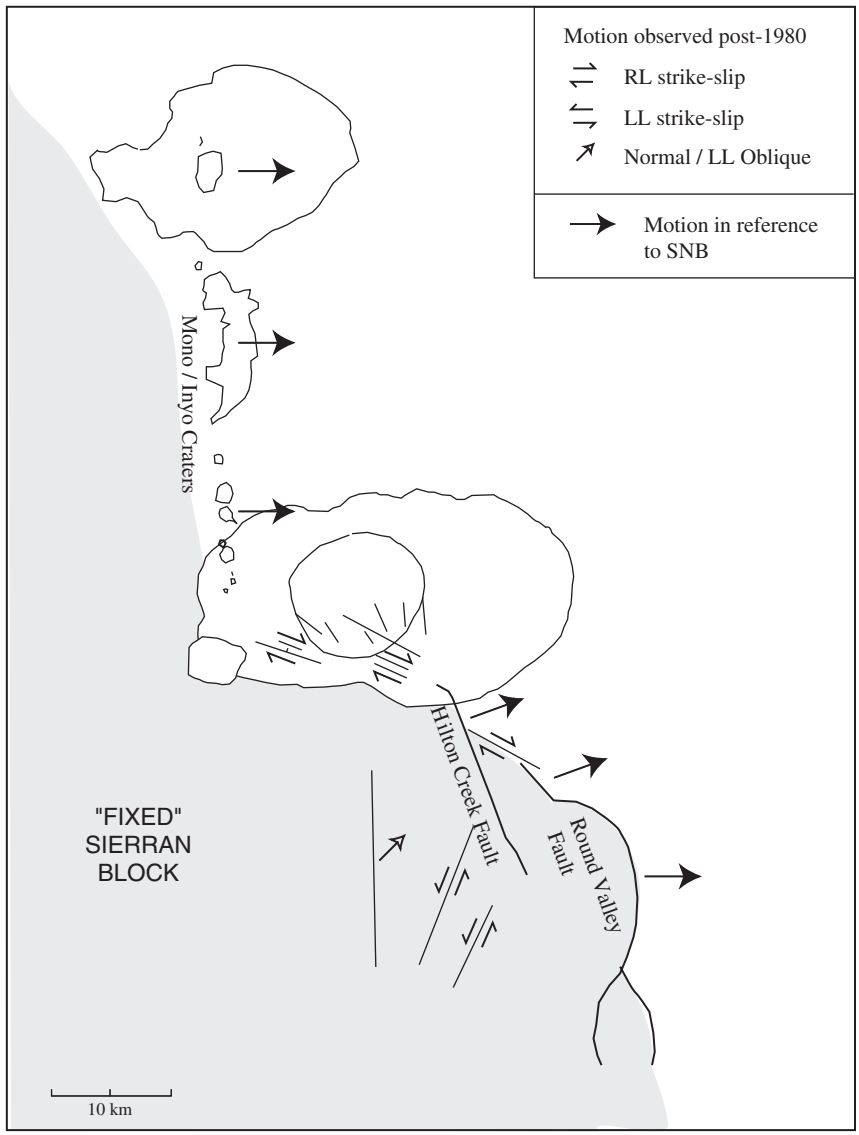

Figure 14. Schematic map of Long Valley area kinematics. Large solid arrows show motion in reference to a stationary SNB. Small open arrows show relative motion on faults. The southern caldera forms a right-lateral ''transform'' zone in the left step between locales of extension, which are shown by solid arrows with reference to a stable Sierra Nevada.

[43] To test this possibility, we constructed a model of normal slip on the Hilton Creek fault and E-W opening along the Mono/Inyo dike that represents deformation of these structures over about the last 1000 years. The purpose of this model is to investigate the state of stress in the Long Valley caldera area resulting from the interaction of extension across these two structures. Thus, the model assumes that local extension has occurred relatively recently, such that any stress perturbations caused by the interaction of these structures have not yet relaxed. We imposed a maximum of 6 m of pure normal slip on the Hilton Creek fault and a maximum of 10 m of E-W opening across the Mono/Inyo dike and simplified the geometry of these features (Figure 15). The Hilton Creek fault is modeled by a fault dipping 60°N 60°E, which extends slightly into the caldera. The Mono/Inyo dike is modeled as a vertically opening feature extending from Mono Lake to ~5 km beyond the Red Cones (Figure 2). Displacement across both the dike and the fault is tapered to zero at the top and sides, and both features are assumed to cut through the entire crust and the upper mantle. Realistically, extension across these discrete structures occurs over a more limited depth range. However, because the lower crust at the base of the seismogenic zone is not truly elastic, as is assumed in our model, we extended displacement to great depth to avoid unrealistic stress concentrations at the base of the faults. Models in which displacement only occurs through the seismogenic upper crust give similar results.

[44] The S_3 directions resulting from extension across these structures are shown in Figure 15. If local effects due to extension across the Hilton Creek fault and Mono/Inyo dike dominate the stress field in the area (Figure 15a), the calculated stress field agrees poorly with observations. If the stresses shown in Figure 15a are superimposed on the back-

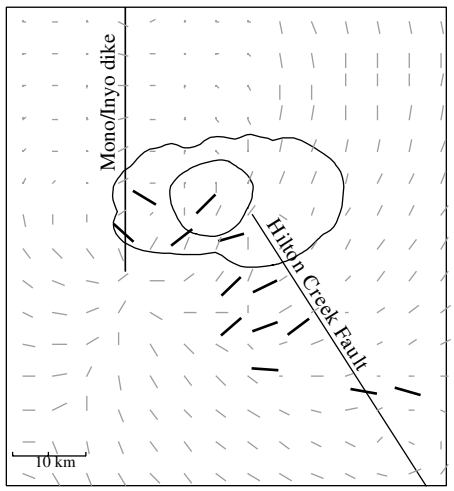

a) S_3 directions due to tectonic step over with dike injection, assuming isotropic stress field.

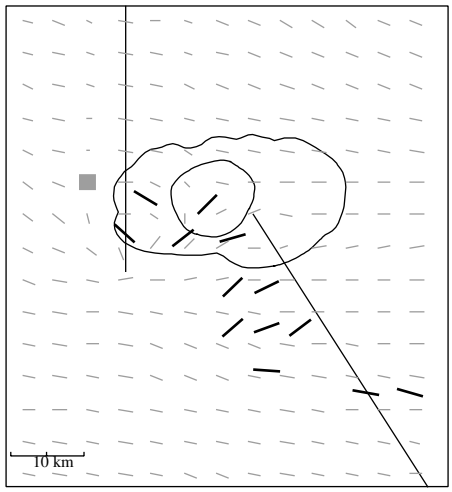

b) S_3 directions due to tectonic step over with dike injection (a) and realistic regional stress field.

Figure 15. Dislocation modeling results of S_3 direction resulting from opening across the Mono/Inyo dike chain and normal slip on the Hilton Creek fault (gray lines). Black lines are S_3 observations for comparison. Line length indicates plunge of S_3 axis and short lines are steeply plunging. (a) S_3 direction due to extension across the Hilton Creek fault and Mono/Inyo dike (no deviatoric stress in the far field). (b) S_3 direction due to extension (shown in (a)) combined with background regional stress field calculated assuming high pore pressure ($Pp = 0.8\ S_V$).

ground regional stress field, local stress perturbations due to extension result in a stress distribution that is reasonably consistent with the observations throughout the caldera, in the southern SNB, and in Round Valley (Figure 15b). Although this model (Figure 15b) does not correctly reproduce stress directions observed in the SNB just south of the caldera, overall, it fits the observations fairly well.

[45] These simple models obviously overlook additional sources of stress in the caldera area (such as other inflational sources, dikes, faults, etc.) that might explain the discrepancies between the models presented here and the observations. Also, because the details of the calculated stress distributions are strongly dependent on the details of the models, such as the fault displacement distributions, the background stress field, and crustal rheology, adjusting model parameters could lead to results more consistent with the observations, particularly in the case of the tectonically driven stress perturbation with high pore pressure (Figure 15b). For example, if we have underestimated the pore pressure or overestimated the magnitudes of the regional stresses in the SNB in the model shown in Figure 15b, S_3 would be more strongly rotated to the NE in this area (Figure 15a) and would therefore be more consistent with the observations. However, we do not choose to adjust model parameters arbitrarily to improve consistency between the model and data.

[46] Because the true details of the distribution of crustal properties, the distribution of tectonic activity, and the magnitudes of the regional stresses at depth are unknown, we cannot correctly resolve the extent or the magnitude of the stress rotation across the south moat created by tectonic activity. Thus, the tectonically driven model is somewhat speculative and poorly constrained. However, in the tectonically driven model the general direction of the stress perturbations created by the step over in Sierran bounding extension is consistent with observations, whereas the stress perturbations created by the inflation-driven model are not consistent with observations.

5. Conclusions

[47] Relocations using the double-difference method [*Waldhauser and Ellsworth*, 2000] reveal an intricate fabric of faults in the south moat and southern resurgent dome of the caldera that have been active since 1980. The imaged faults are summarized in Table 2. The dominant fault zone, which has accommodated most of the recent seismic moment in the caldera, forms the southern boundary of caldera seismicity and consists of several subparallel right-lateral strike-slip faults, oriented roughly N70°W/80°NE. Many smaller strike-slip faults with more northerly strikes (maximum strike of N06°W) are active to the north of the main south moat fault zone. Caldera faults tend to rupture in brief, intense seismic swarms.

[48] Seismicity in the Sierra Nevada basement south of the caldera is largely confined to an east-dipping north/south-striking normal/left-lateral fault and to faults within its hanging wall. This active normal fault is located ~10 km inside the Sierra Nevada from the major range bounding Hilton Creek fault. Two N28°E-striking left-lateral strike-slip faults dominate hanging wall seismicity.

[49] Stress inversions reveal that the direction of minimum compressive stress systematically rotates across the studied region, from a NE–SW relative extension direction in the south moat of the caldera, to a WNW–ESE relative extension direction in Round Valley, 25 km SE of the caldera. Because WNW–ESE extension is characteristic

of the western boundary of the Basin and Range province, the stress rotation in the vicinity of the caldera appears to reflect a local stress perturbation centered near the caldera south moat area. This stress perturbation does not appear to result from magma chamber inflation beneath the center of the resurgent dome, but may reflect the large-scale left-step offset in the Sierran range bounding normal faults. Thus, although magmatic activity may trigger earthquakes in the Long Valley area, the direction of fault slip seems to be controlled by regional tectonic processes rather than local magmatic processes.

[50] **Acknowledgments.** We are grateful to Dave Hill, George Thompson, and Roy Bailey for sharing their knowledge about the Long Valley caldera in stimulating discussions. We also thank Ross Stein for his time and advice on using Coulomb 2.0 software and Jim Savage, Fred Pollitz, and two anonymous reviewers for their helpful reviews.

References

Angelier, J., Determination of the mean principal directions of stresses for a given fault population, *Tectonophysics*, *56*, T17–T26, 1979.

Bailey, R., Geologic map of the Long Valley caldera, Mono–Inyo craters volcanic chain, and vicinity, eastern California, *U.S. Geol. Surv. Misc. Geol. Invest. Map*, I-1933, 1989.

Battaglia, M., C. Roberts, and P. Segall, Magma intrusion beneath Long Valley caldera confirmed by temporal changes in gravity, *Science*, *285*, 2119–2122, 1999.

Bellier, O., and M. L. Zoback, Recent state of stress change in the Walker Lane zone, western Basin and Range province, United States, *Tectonics*, *14*, 564–593, 1995.

Bursik, M., and K. Sieh, Range front faulting and volcanism in the Mono Basin, eastern California, *J. Geophys. Res.*, *94*, 15,587–15,609, 1989.

Clark, M. M., and A. R. Gillespie, Record of late Quaternary faulting along the Hilton Creek fault in the Sierra Nevada, California, *SSA Earthquake Notes*, *52*, 46, 1981.

Dreger, D. S., H. Tkalcic, and M. Johnston, Dilatational processes accompanying earthquakes in the Long Valley caldera, *Science*, *288*, 122–125, 2000.

Eichelberger, J. C., C. R. Carrigan, H. R. Westrich, and R. H. Price, Non-explosive silicic volcanism, *Nature*, *323*, 598–602, 1986.

Ekström, G., Evidence for source complexities of 1980 Mammoth Lakes earthquakes, *Eos Trans. AGU*, *64*, 769, 1983.

Gephart, J. W., Stress and the direction of slip on fault planes, *Tectonics*, *9*, 845–858, 1990a.

Gephart, J. W., FMSI: A FORTRAN program for inverting fault/slickenside and earthquake focal mechanism data to obtain the regional stress tensor, *Comput. Geosci.*, *16*, 953–989, 1990b.

Gephart, J. W., and D. W. Forsythe, An improved method for determining the regional stress tensor using earthquake focal mechanism data: Application to the San Fernando earthquake sequence, *J. Geophys. Res.*, *89*, 9305–9320, 1984.

Given, J. W., T. C. Wallace, and H. Kanamori, Teleseismic analysis of the 1980 Mammoth Lakes earthquake sequence, *Bull. Seismol. Soc. Am.*, *72*, 1093–1109, 1982.

Hardebeck, J. L., and E. Hauksson, Stress orientations obtained from earthquake focal mechanisms: What are appropriate uncertainty estimates?, *Bull. Seismol. Soc. Am.*, *91*, 250–262, 2001.

Hill, D. P., E. Kissling, J. H. Luetgert, and U. Kradolfer, Constraints on the upper crustal structure of the Long Valley-Mono Craters volcanic complex, eastern California, from seismic refraction measurements, *J. Geophys. Res.*, *90*, 11,135–11,150, 1985.

Hill, D. P., W. L. Ellsworth, M. J. S. Johnston, J. O. Langbein, D. H. Oppenheimer, A. M. Pitt, P. A. Reasenberg, M. L. Sorey, and S. R. McNutt, The 1989 earthquake swarm beneath Mammoth Mountain, California: An initial look at the 4 May through 30 September activity, *Bull. Seismol. Soc. Am.*, *80*, 325–339, 1990.

Hill, D. P., et al., Response plans for volcanic hazards in the Long Valley caldera and Mono craters area, California, *U.S. Geol. Surv. Bull.*, *2185*, 21–44, 2002.

Julian, B. R., and S. A. Sipkin, Earthquake processes in the Long Valley caldera area, California, *J. Geophys. Res.*, *90*, 11,155–11,169, 1985.

Julian, B. R., G. R. Foulger, A. M. Pitt, D. P. Hill, P. E. Malin, and E. Shalev, Earthquake mechanisms at Long Valley caldera, California, *Eos Trans. AGU*, *81*, F1384, 2000.

Langbein, J., Deformation of the Long Valley caldera, eastern California from mid-1983 to mid-1988: Measurements using a two-color geodimeter, *J. Geophys. Res.*, *94*, 3833–3849, 1989.

Langbein, J., D. Dzurisin, G. Marshall, R. Stein, and J. Rundle, Shallow and peripheral volcanic sources of inflation revealed by modeling two-color geodimeter and leveling data from Long Valley caldera, California, 1988–1992, *J. Geophys. Res.*, *100*, 12,487–12,495, 1995.

Lee, W. H. K., and J. C. Lahr, HYPO71 (revised): A computer program for determining hypocenter, magnitude, and first motion pattern of local earthquakes, *U.S. Geol. Surv. Open File Rep.*, *75-311*, 100 pp., 1975.

Marshall, G. A., J. Langbein, R. S. Stein, M. Lisowski, and J. Svarc, Inflation of Long Valley caldera, California, Basin and Range strain, and possible Mono Craters dike opening from 1990–94 GPS surveys, *Geophys. Res. Lett.*, *24*, 1003–1006, 1997.

McKenzie, D. P., The relation between fault plane solutions for earthquakes and the directions of the principal stresses, *Bull. Seismol. Soc. Am.*, *59*, 591–601, 1969.

Michael, A. J., Use of focal mechanisms to determine stress: A control study, *J. Geophys. Res.*, *92*, 357–368, 1987.

Moos, D., and M. D. Zoback, State of stress in the Long Valley caldera, California, *Geology*, *21*, 837–840, 1993.

Prejean, S. G., *The interaction of tectonic and magmatic processes in the Long Valley caldera, California*, Ph.D. dissertation, 131 pp., Stanford Univ., Stanford, Calif., 2002.

Reasenberg, P. A., and D. Oppenheimer, FPFIT, FPPLOT, and FPPAGE: Fortran computer programs for calculating and displaying earthquake fault-plane solutions, *U.S. Geol. Surv. Open File Rep.*, *85-739*, 27 pp., 1985.

Savage, L. C., and R. S. Cockerham, Earthquake swarm in Long Valley caldera, California, January 1983: Evidence for dike inflation, *J. Geophys. Res.*, *89*, 8315–8324, 1984.

Savage, J. C., and M. Lisowski, Strain accumulation in Owens Valley, California, 1974 to 1988, *Bull. Seismol. Soc. Am.*, *85*, 151–158, 1995.

Schaff D. P., G. H. R. Bokelmann, G. C. Beroza, F. Waldhauser, and W. L. Ellsworth, High resolution image of Calaveras Fault seismicity, *J. Geophys. Res.*, *107*(B9), 2186, doi:10.1029/2001JB000633, 2002.

Simons, M., Y. Fialko, L. Rivera, E. Chapin, S. Hensley, P. A. Rosen, S. Shaffer, F. H. Webb, and J. Langbein, Analysis of geodetic measurements of crustal deformation at Long Valley caldera, *Eos Trans. AGU*, *81*, F1322, 2000.

Smith, K. D., and K. F. Priestly, The foreshock sequence of the 1986 Chalfant, California, earthquake, *Bull. Seismol. Soc. Am.*, *78*, 172–187, 1988.

Toda, S., R. S. Stein, P. A. Reasenberg, and J. H. Dieterich, Stress transferred by the Mw = 6.5 Kobe, Japan, shock: Effect on aftershocks and future earthquake probabilities, *J. Geophys. Res.*, *103*, 24,543–24,565, 1998.

Townend, J., and M. D. Zoback, How faulting keeps the crust strong, *Geology*, *28*, 399–402, 2000.

Vetter, U. R., and A. S. Ryall, Systematic change of focal mechanism with depth in the western Great Basin, *J. Geophys. Res.*, *88*, 8237–8250, 1983.

Waldhauser, F., hypoDD: A program to compute double-difference hypocenter locations, *U.S. Geol. Surv. Open File Rep.*, *01-113*, 25 pp., 2001.

Waldhauser, F., and W. L. Ellsworth, A double-difference earthquake location algorithm: Method and application to the northern Hayward fault, California, *Bull. Seismol. Soc. Am.*, *90*, 1353–1368, 2000.

Waldhauser, F., and W. L. Ellsworth, Fault structure and mechanics of the Hayward Fault, California, from double-difference earthquake locations, *J. Geophys. Res.*, *107*, 2054, doi:10.1029/2001JB000084, 2002.

Wallace, T. C., A reexamination of the moment tensor solutions of the 1980 Mammoth Lakes earthquakes, *J. Geophys. Res.*, *90*, 11,171–11,176, 1985.

Wallace, T., J. Given, and H. Kanamori, A discrepancy between long- and short-period mechanisms of earthquakes near the Long Valley caldera, *Geophys. Res. Lett.*, *10*, 1131–1134, 1982.

Zoback, M. L., State of stress and modern deformation of the northern Basin and Range province, *J. Geophys. Res.*, *94*, 7105–7128, 1989.

W. L. Ellsworth, U.S. Geological Survey, 345 Middlefield Road, MS 910, Menlo Park, CA 94025, USA.

S. Prejean, F. Waldhauser, and M. Zoback, Stanford University, Department of Geophysics, Stanford, CA 94305, USA. (sprejean@usgs. gov)